Nodal-line resonance generating the giant anomalous Hall effect of $Co_3Sn_2S_2$

F. Schilberth,[1,2] M.-C. Jiang,[3,4] S. Minami,[5,6] M. A. Kassem,[7,8] F. Mayr,[1] T. Koretsune,[9] Y. Tabata,[7] T. Waki,[7] H. Nakamura,[7] G.-Y. Guo,[3,10] R. Arita,[4,11] I. Kézsmárki,[1] and S. Bordács[2,12,*]

[1]*Experimentalphysik V, Center for Electronic Correlations and Magnetism, Institute for Physics, Augsburg University, D-86135 Augsburg, Germany*

[2]*Department of Physics, Institute of Physics, Budapest University of Technology and Economics, Műegyetem rkp. 3., H-1111 Budapest, Hungary*

[3]*Department of Physics and Center for Theoretical Physics, National Taiwan University, Taipei 10617, Taiwan*

[4]*RIKEN Center for Emergent Matter Science, 2-1 Hirosawa, Wako 351-0198, Japan*

[5]*Department of Mechanical Engineering and Science, Kyoto University, Nishikyo-ku, Kyoto 615-8540, Japan*

[6]*Department of Physics, University of Tokyo, Bunkyo-ku, Tokyo 113-0033, Japan*

[7]*Department of Materials Science and Engineering, Kyoto University, Kyoto 606-8501, Japan*

[8]*Department of Physics, Faculty of Science, Assiut University, 71516 Assiut, Egypt*

[9]*Department of Physics, Tohoku University, Sendai 980-8578, Japan*

[10]*Physics Division, National Center for Theoretical Sciences, Taipei 10617, Taiwan*

[11]*Research Center for Advanced Science and Technology, University of Tokyo, 4-6-1 Meguro-ku, Tokyo 153-8904, Japan*

[12]*ELKH-BME Condensed Matter Research Group, Budapest University of Technology and Economics, Műegyetem rkp. 3., H-1111 Budapest, Hungary*

(Received 28 February 2023; accepted 5 June 2023; published 27 June 2023)

Giant anomalous Hall effect (AHE) and magneto-optical activity can emerge in magnets with topologically nontrivial degeneracies. However, identifying the specific band-structure features such as Weyl points, nodal lines, or planes which generate the anomalous response is a challenging issue. Since the low-energy interband transitions can govern the static AHE, we addressed this question in the prototypical magnetic Weyl semimetal $Co_3Sn_2S_2$ also hosting nodal lines by broadband polarized reflectivity and magneto-optical Kerr effect spectroscopy with a focus on the far-infrared range. In the linear dichroism spectrum we observe a strong resonance at 40 meV, which also appears in the optical Hall conductivity and primarily determines the static AHE, and thus confirms its intrinsic origin. Our material-specific theory reproduces the experimental data remarkably well and shows that strongly tilted nodal-line segments around the Fermi energy generate the resonance. While the Weyl points only give vanishing contributions, these segments of the nodal lines gapped by the spin-orbit coupling dominate the low-energy optical response and generate the giant AHE.

DOI: 10.1103/PhysRevB.107.214441

I. INTRODUCTION

Topological Dirac and Weyl semimetals have received much attention, since at low energies their electrons mimic relativistic particles [1]. Moreover, topological semimetals with higher dimensional degenerate manifolds, such as nodal lines or planes, have been predicted and observed, which host quasiparticles that are unprecedented in particle physics [2–5]. These peculiar band-structure features give rise to e.g. exceptionally high mobility [6,7], chiral anomaly [8,9], Fermi arcs and drumhead surface states [10–13], and unusual quantization of orbital motion in a magnetic field [14,15].

Recently, the search for such topological band features in magnetic materials has become a hot topic. In magnets, the topological nodes can be controlled by magnetic fields [16–18], they induce exotic domain wall states [19,20], and generate enhanced anomalous Hall effect (AHE) [1,21]. The intrinsic AHE being proportional to the Berry curvature integrated over the Brillouin zone (BZ) is of particular importance as it is a direct consequence of the nontrivial band topology [22]. At the heart of these phenomena, there is the interplay between the magnetic order and the band structure mediated by the spin-orbit coupling (SOC). In the ordered state, the broken spin-rotation symmetry may either reduce the degeneracy of the manifolds, e.g., transform a nodal line into Weyl points [23,24], or completely gap out the nodes, which may stabilize a topological insulator phase [25]. Therefore, from the many band-structure features, pinpointing those responsible for the anomalous responses is highly desirable.

This is an especially important question in the prototypical magnetic Weyl semimetal $Co_3Sn_2S_2$ with individual Weyl points remaining degenerate from SOC gapped nodal loops. Its crystal structure (space group $R\bar{3}m$) consists of an *ABC*-type stack of Co_3Sn kagome layers, and belongs to the family of shandites [26]. Below $T_c = 177$ K, a ferromagnetic order develops with the moments aligned towards the *c* axis at low temperatures. Just below the transition,

*bordacs.sandor@ttk.bme.hu

an anomalous magnetic phase with noncollinear order was proposed [27,28], but more recent experiments suggest that the domain configuration changes instead [29,30]. Due to its kagome structure, $Co_3Sn_2S_2$ possesses nontrivial electronic topology. In addition to flat bands [31,32], nonrelativistic density functional theory (DFT) calculations propose nodal loops on high-symmetry planes of the BZ, which become gapped upon including SOC, each leaving behind a pair of Weyl nodes [33–35]. Angle-resolved photoemission spectroscopy (ARPES) studies confirmed the existence of the nodal line and Fermi arcs in this system [35–37] and chiral edge modes were found in scanning tunneling microscopy [38]. The Berry curvature accumulated by the anticrossing line is claimed to be the source of large anomalous Hall and Nernst effects in this material [23,34], while others suggest that the Weyl nodes are responsible for the AHE [33]. Its magnitude reaches as high as 1200 Ω^{-1} cm^{-1} and is therefore comparable to the AHE in the related compound Fe_3Sn_2 [39,40], in which, as demonstrated recently, only a fraction of the intrinsic AHE can be attributed to twisted nodal lines [41]. Therefore, although the DFT band structure of $Co_3Sn_2S_2$ is relatively simple close to the Fermi level, it is to date unclear which band-structure feature dominates the AHE—the gapped nodal loop or the Weyl points.

Here, we address this fundamental question and determine the full optical conductivity tensor of $Co_3Sn_2S_2$ by polarized infrared reflectivity and magneto-optical Kerr effect (MOKE) spectroscopy:

$$\hat{\sigma}(\omega) = \begin{bmatrix} \sigma_{xx}(\omega) & \sigma_{xy}(\omega) & 0 \\ -\sigma_{xy}(\omega) & \sigma_{xx}(\omega) & 0 \\ 0 & 0 & \sigma_{zz}(\omega) \end{bmatrix}. \quad (1)$$

For simplicity and readability, we omit the explicit frequency dependence for the rest of the paper.

Our results indicate that linear dichroism, evaluated by the ratio of the conductivity in the kagome plane, σ_{xx}, and out-of-plane, σ_{zz}, is a sensitive probe of topological features of layered materials. We find a resonant enhancement of the linear dichroism due to transitions along the gapped nodal line. We reveal a giant magneto-optical activity in the same energy range by extending MOKE spectroscopy down to $\hbar\omega = 25$ meV. Specifically, we observe (1) a resonance peak at 40 meV in the Hall conductivity spectrum, σ_{xy}, which has not been detected before, and (2) directly capture the fingerprints of the nodal loop in the optical conductivity without any extrapolation of σ_{xy}. We highlight that MOKE spectroscopy is a bulk-sensitive, direct probe of the interband transitions responsible for the Berry curvature and the intrinsic AHE, which is information not available for ARPES. Complemented by *ab initio* calculations, we analyze the momentum space distribution of the Hall spectral weight, which allows us to disentangle the contributions of the gapped nodal line and Weyl points.

II. EXPERIMENTAL METHODS

For the magneto-optical measurements, a large single crystal of $Co_3Sn_2S_2$ was grown in a cylindro-conical shape (1 cm in diameter and 5 cm in length) from its melt by a modified Bridgman method [42–44]. About 10 g of polycrystalline

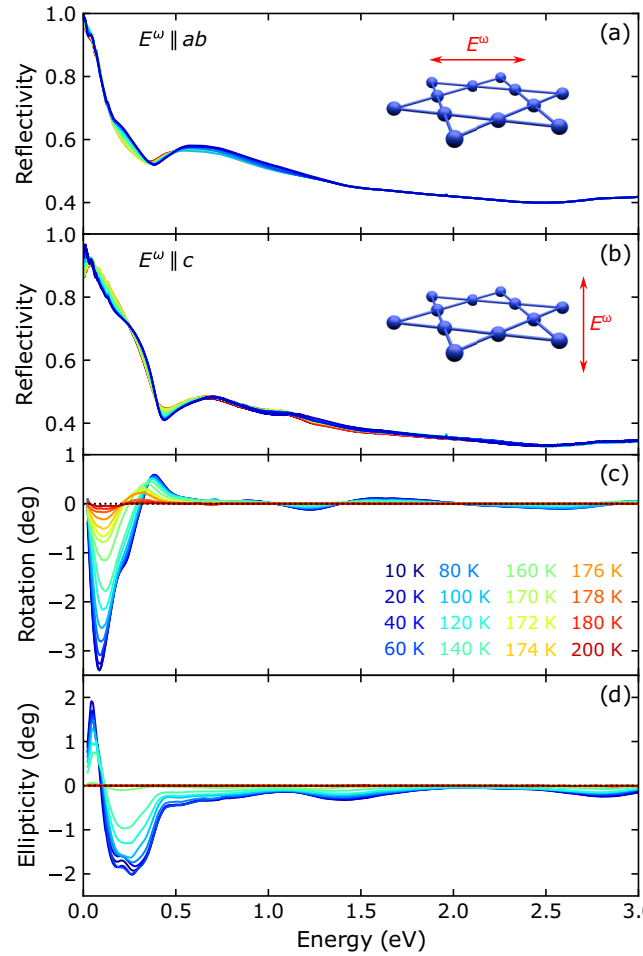

FIG. 1. Optical spectra measured for several temperatures between 10 and 200 K of (a) the reflectivity on the kagome plane and (b) along the stacking direction. The insets highlight the orientation of the electric field. (c) Kerr-rotation and (d) ellipticity on the *ab*-plane in the energy range up to 3 eV.

$Co_3Sn_2S_2$ synthesized by a solid state reaction was charged in a tipped glassy carbon crucible which was sealed under vacuum in a quartz tube. The sealed ampule was suspended by a Kanthal thread from the top to the hot zone of a vertical tube furnace and heated over 30 hours up to 1000 °C, kept for 6 h, and then slowly cooled over 72 h to 800 °C. After furnace cooling, the crystal was removed from the crucible and could be easily cleaved in the (001) plane. Crushed parts were investigated by powder x-ray diffraction, Laue x-ray spectroscopy and wave-length dispersive x-ray spectroscopy, those indicated a single-phase and high-quality grown crystal with stoichiometric chemical composition of $Co_3Sn_2S_2$.

Polarized reflectivity spectra were measured on cut and polished *ab* and *ac* surfaces with a lateral size of ∼5 and ∼3 mm, respectively. The spectra were obtained in a Bruker IFS/66 FTIR-spectrometer for the MIR-VIS range and a Bruker Vertex 80v for the FIR. The spectra were measured in the frequency range 80-32000 cm^{-1} (0.01–4 eV) from room temperature down to 10 K. As references, a silver and gold mirror where used in the MIR-VIS and FIR experiments, respectively. The optical conductivity σ_1 was calculated by

using Kramers-Kronig analysis on the merged spectra. At this point, the low-energy side of the reflectivity spectrum was extrapolated by using a Hagen-Rubens law and the dc-conductivity, while for the UV the reflectivity spectrum was extrapolated with free electron behaviour setting in at $10^6\,\mathrm{cm}^{-1}$ and an exponent for the interband regime of 1.5.

The broadband MOKE spectra were recorded in near-normal incidence and were combined from several measurements in different frequency ranges, employing grating and interferometer based spectrometers as described elsewhere [41,45–47]. Small permanent magnets provided a field of ±0.3 T at the sample position. A schematic of the MIR–MOKE setup is shown in Fig. S2. Because of the large uniaxial anisotropy in this material, the sample was cooled across T_c in positive and negative fields to ensure complete reversal of the magnetic domains. The Hall conductivity spectra were calculated using the complex Kerr rotation (0.025–3 eV) according to

$$\theta + i\eta = -\frac{\sigma_{xy}}{\sigma_{xx}\sqrt{1 + i\frac{1}{\varepsilon_0\omega}\sigma_{xx}}}, \tag{2}$$

where ω is the angular frequency of the photon and ϵ_0 is the vacuum permittivity.

III. DFT CALCULATIONS

The electronic structure of $Co_3Sn_2S_2$ was calculated using the Vienna ab initio simulation package (VASP) based on the DFT [48–50]. The generalized gradient approximation of Perdew-Burke-Ernzerhof was adopted for the exchange-correlation functional [51]. For the crystal structure for $Co_3Sn_2S_2$ the experimentally determined lattice parameters were used with $a = 5.379\,\text{Å}$ and $\alpha = 59.8658°$ [52]. In the self-consistent band structure calculations, Γ-centered k meshes of 24 × 24 × 24 were used in the Brillouin zone integration. The optical properties are further evaluated using the Wannier functions, and the Kubo-Greenwood formula [53].

A fine mesh of 400 × 400 × 400 k points are applied during the integration with good convergence. The Wannier functions were constructed using Co d, Sn s, p, and S s, p orbitals with a resulting tight-binding model well describing the DFT band structures (cf. Fig. S2).

IV. EXPERIMENTAL RESULTS

The reflectivity and MOKE spectra measured between 10 and 200 K are included in Fig. 1 of the Supplemental Material [42]. The out-of-plane reflectivity remarkably differs from the in-plane spectrum, the latter being in agreement with earlier reports [32,54]. In the overlapping energy range, the MOKE spectra agree with those published in Ref. [55]. Beside the giant Kerr rotation with a peak magnitude of −3.3° at 0.09 eV, we resolve a peak around 50 meV in the ellipticity with a magnitude of 2°, which was not detected before. Importantly, our Kerr rotation and ellipticity obey the Kramers-Kronig relation and fulfill the magneto-optical sum rule, requiring that both parameters approach 0 for $\omega \to 0$.

We show the low-energy spectrum for each independent component of the optical conductivity tensor in Fig. 2 (a broad energy range is shown in the respective inset). The corresponding static conductivity values are shown for comparison and agree well with the respective spectra at the low-energy cutoff. In panel (a), the real part of σ_{xx} exhibits a Drude-like increase towards zero energy responsible for the static conductivity. At 30 meV, a peak is forming below 100 K, separated well from the free-carrier response. For even higher energies, we find a small temperature-dependent hump around 0.25 eV and a step edge around 0.6 eV before the conductivity becomes flat without significant temperature dependence. These features agree with earlier reports [32,54,55].

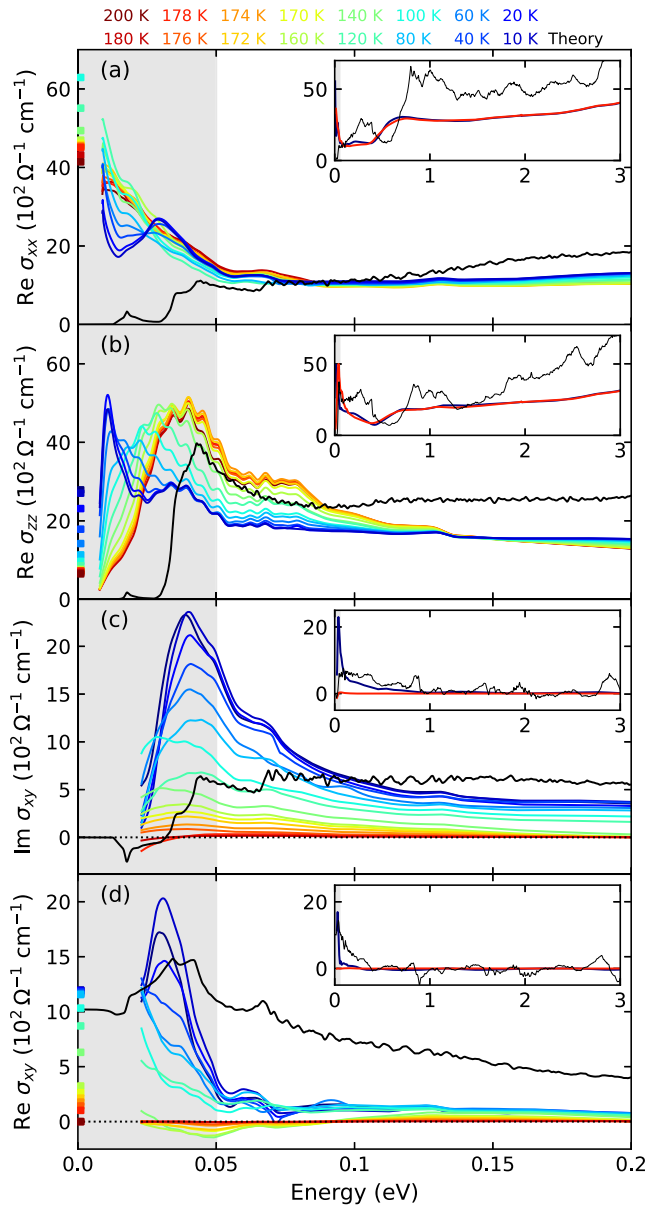

FIG. 2. Comparison of the experimental conductivity spectra measured between 10 and 200 K (colored lines) and the theoretical DFT spectra (black lines) calculated as described in the text. (a), (b), (c), and (d) respectively show the real parts of the diagonal, Re σ_{xx} and Re σ_{zz}, as well as the imaginary and real parts of the off-diagonal conductivity spectra, Im σ_{xy} and Re σ_{xy}. For comparison, the static conductivity values are plotted as colored squares at zero energy. The respective insets show a broad energy range.

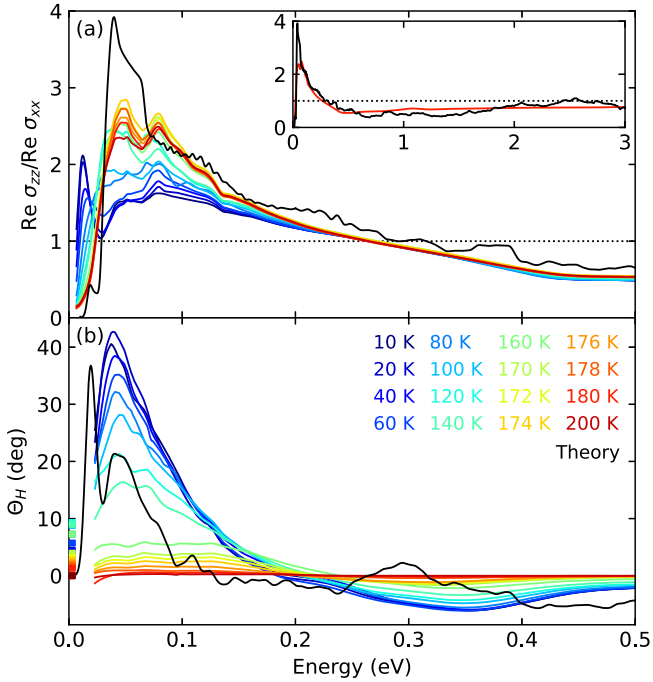

FIG. 3. (a) Optical anisotropy spectra $\mathrm{Re}\,\sigma_{zz}/\mathrm{Re}\,\sigma_{xx}$. The inset shows a broader energy range. (b) Hall angle spectra $\Theta_\mathrm{H} = \arctan \mathrm{Re}(\sigma_{xy}/\sigma_{xx})$ with a maximum of 42.7°.

The out-of-plane conductivity spectrum, σ_{zz} in panel (b), strongly deviates from σ_{xx}. Most strikingly, no sign of a Drude peak is observed down to our low-energy cutoff, and the dc conductivity is also much lower for this direction, indicated by the colored squares at zero energy. Therefore, we suspect that within the kagome planes, the strong orbital overlap between Co sites can produce a coherent conduction, manifested in the Drude term. In contrast, the transport is likely due to incoherent hopping perpendicular to the planes [56]. We find a peak at 40 meV, which broadens and shifts to lower energies upon lowering the temperature, before it eventually splits in two below 80 K. At higher energies, we find a minimum at 0.4 eV, which becomes sharper at low temperatures, and a step edge at 0.6 eV. For even higher energies, σ_{zz} is featureless though slightly increasing without distinct temperature dependence, similar to σ_{xx} [see inset of panel (b)].

In Figs. 2(c) and 2(d), the Hall conductivity spectrum σ_{xy} shows a strong resonance at 40 meV, in coincidence with the in- and out-of-plane diagonal components and their ratio (cf. Fig. 3). We emphasize that this far-infrared range has not been covered so far, while the higher energy part of the spectra agree very well with Ref. [55]. Both the imaginary and real parts exhibit a large enhancement towards low temperatures, where the peak in the real part overshoots the dc AHE below 60 K with a magnitude as high as 2000 $\Omega^{-1}\,\mathrm{cm}^{-1}$ at 10 K. The good agreement between the low-energy tail of the real part of σ_{xy} and the dc AHE together with the formerly published featureless terahertz data [55], suggests that there are no further excitations in the narrow uncovered energy window. Furthermore, as the scattering rate obtained from the Drude peak for σ_{xx} is below the cutoff for σ_{xy}, we conclude that the giant anomalous Hall conductivity of $Co_3Sn_2S_2$ has dominantly intrinsic origin and it is generated by the interband resonance observed here.

V. AB INITIO ANALYSIS

In order to reveal the microscopic origin of the observed spectral features, we performed *ab initio* calculations providing all symmetry-allowed elements of the conductivity tensor [57]. The theoretical spectra are coplotted with the experiment in Fig. 1. Disregarding the intraband contribution that is not included in the theory, the spectra qualitatively reproduce all conductivity components on a large energy scale, although the spectral features appear slightly shifted to higher energies compared to experiment, which may indicate correlation effects [32].

We quantified the linear dichroism for in- and out-of-plane polarizations by calculating $\mathrm{Re}\,\sigma_{zz}/\mathrm{Re}\,\sigma_{xx}$ from the spectra shown in Fig. 1. As demonstrated in Fig. 2, the theory agrees with the experiment remarkably well, especially at higher temperatures. We find that around the resonance at 40 meV, σ_{zz} becomes three times larger than σ_{xx}. As the temperature is decreased in the experiment, some of the spectral weight splits and moves to lower energies. Although this is not properly captured by the DFT calculations, the overall tendency, that σ_{zz} is stronger at the resonances, remains valid. The optical anisotropy is closely related to the selection rules, which depend on the irreducible representations of the dipole operators as well as the initial and final states within the underlying point group [58]. For instance, a dipole operator with a trivial representation would only allow transitions between states of the same orbital character. Interestingly, in topological materials, the presence of protected crossing points prevents hybridization, enabling clear differentiation of anisotropy through the selection rules. As the Kubo formalism accurately describes the low-frequency anisotropy spectra in the current project, it suggests optical anisotropy as a potentially new signature of nontrivial topological band structures. Detailed derivations and the generality of such signatures in all topological materials are beyond the scope of the current project but will be kept as a future direction.

The Hall conductivity is also well reproduced by theory as shown in Figs. 2(c) and 2(d). The imaginary part shows a sudden increase at 40 meV, where the resonance is observed in the experiment, though it is not that pronounced. Importantly, the theory properly captures the 34.3 meV peak in $\mathrm{Re}\,\sigma_{xy}$. The experimental feature is somewhat sharper like in the case of the imaginary part, which may again be related to electronic correlations [32]. The dc extrapolation of the theory yields the same AHE as the magnetotransport measurements. Backed with this remarkable agreement, we now analyze the band-structure origin of this giant optical Hall effect signal.

We deduced the momentum decomposition of the off-diagonal conductivity by introducing the Hall spectral weight $H_{xy}(\omega, \mathbf{k})$ as $\sigma_{xy}(\omega) = ie^2/\hbar V \int_{BZ} H_{xy}(\omega, \mathbf{k})$. [For details see Eq. (S1) and the text of the Supplemental Material [59].] Figure 4(b) shows the Hall spectral weight of the 34.3 meV low-energy peak in $\mathrm{Re}\,\sigma_{xy}$ on one of the mirror planes containing the nodal line and the Weyl points as indicated by the rainbow line and black labels, respectively [34,60]. The black line is the border of the BZ, the green lines plot the

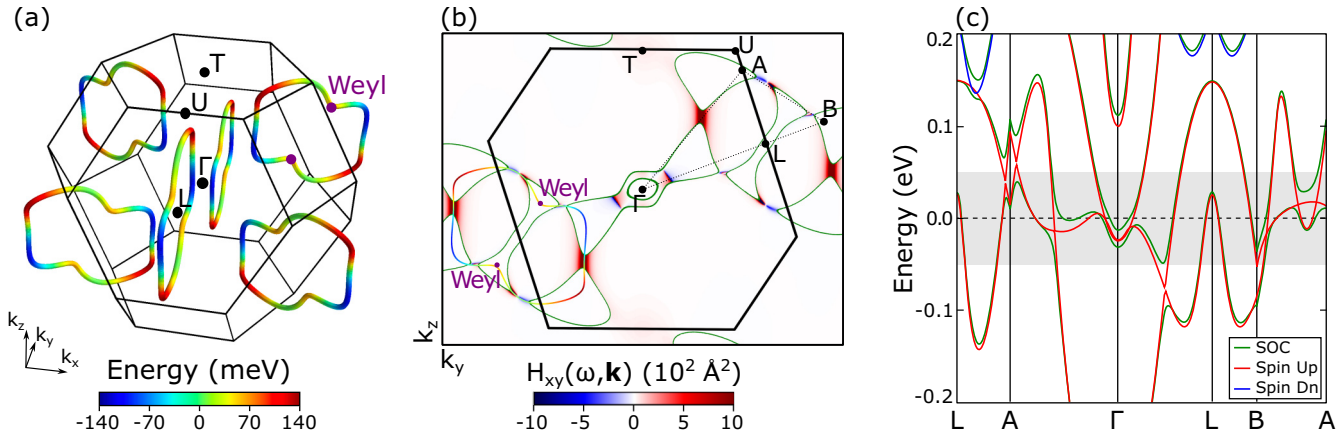

FIG. 4. (a) Location of the nodal lines and the Weyl nodes in the Brillouin zone. The color scale encodes the position relative to the Fermi energy. (b) The Hall spectral weight of the calculated 34.3-meV peak on the mirror plane containing the nodal line and Weyl points. (c) Band structure along the main contributing areas of the real part of the off-diagonal optical conductivity. The gray shading highlights the energy range below 50 meV where we expect contributions to the peak in Re σ_{xy}. The non-high-symmetry points A and B are (0.0, 0.4002, 0.301) and (0.0, 0.7373, 0.0) in reciprocal lattice units.

Fermi surface, and the color map presents the spectral weight. For better orientation, panel (a) plots the nodal lines where the coloring encodes the position of the band crossing relative to the Fermi energy. To exempt the contribution from other parts of the BZ, we also checked the Fermi surface of $Co_3Sn_2S_2$ to confirm that no accidental crossings appear around the Fermi level in locations away from the focused mirror plane.

We find several hotspots of Hall conductivity on the slice of the BZ. Interestingly, there is no significant contribution from the Weyl points as they are located 60 meV above the Fermi energy and cannot contribute to the response in the range below [34,60]. Instead, we find regions close to Γ and in the vicinity of A with positive and negative weights right next to each other. Since the conductivity is determined by integration over the BZ, the opposite weight from these points cancels to a large extent. This leaves the large positive patch on the Γ-A line giving the dominant contribution. Aside from the regions around Γ, we always observe a hot spot when the nodal line comes close to or crosses the Fermi energy (light-green segments of the loop), hence the hotspots always connect two close regions of the Fermi surface (dark-green lines).

Although the hot spots seem to have a similar origin, they behave differently in producing optical weight. In order to see the underlying shape of the bands, we introduce two non-high-symmetry points A and B, to plot the band structure along cuts through the hot spots, shown in Fig. 3(c) with and without SOC. The gray shading indicates the relevant low-energy range in the same fashion as in Fig. 1. Along the B-A line, we cut through a hot spot with subsequent positive and negative weights. Here, the two red spin-up bands forming the nodal line are close to the Fermi energy, so with SOC, one of the bands is filled and the other is empty in between the crossings, allowing the optical transitions. Importantly, the tilt of the crossing points is opposite, which is the reason for the different signs of their contribution to σ_{xy} [61,62]. Around Γ, we have a similar situation where two red spin-up band inversions appear with opposite tilt. The SOC opens a gap, which allows transitions once the upper band is above the Fermi energy, also producing an optical Hall response.

The situation must be different along the A-Γ line, where the large positive hot spot does not have a negative partner nearby. Here, we observe only one strongly tilted crossing. Again, with SOC the upper band is pushed above the Fermi level enabling the transition. Due to the strong tilt, the two bands stay nearly parallel over a relatively broad k interval, so the Berry curvature of the gapped nodal line is summed up over a narrow energy range that produces the large patch of optical weight. By inversion and threefold rotation symmetry, we expect a total of six such spots in the BZ dominating the anomalous Hall conductivity.

Since the interband transition from this feature also gives rise to diagonal conductivity, we directly compare σ_{xx} and σ_{xy} by calculating the Hall angle, $\Theta_H = \arctan \mathrm{Re}(\sigma_{xy}/\sigma_{xx})$, which is shown in Fig. S3. At 40 meV, the giant off-diagonal conductivity has almost the same magnitude as the diagonal conductivity producing a very large Hall angle of 42.7°. When the Kubo formula is written using the circular momentum operators $p_\pm = p_x \pm i p_y$,

$$\mathrm{Im}\sigma_{xy} = \frac{e^2\pi}{4m^2V\hbar}\sum_{\mathbf{k},n,n'}\frac{|f[\varepsilon_n(\mathbf{k})] - f[\varepsilon'_n(\mathbf{k})]|}{\omega_{nn'}}\delta(\omega-\omega_{nn'}) \times [|\langle n,\mathbf{k}|p_+|n',\mathbf{k}\rangle|^2 - |\langle n,\mathbf{k}|p_-|n',\mathbf{k}\rangle|^2], \quad (3)$$

σ_{xy} depends on the difference of the two circular components, whereas σ_{xx} is given by their sum [63]. As a consequence, the largest possible Hall angle for an interband transition is 45°. This is realized when one matrix element is zero, which indicates an almost fully polarized transition in the present case, yielding a nodal line resonance.

VI. SUMMARY AND CONCLUSIONS

In summary, we provide a showcase for disentangling the contributions of various topological features to the AHE, and identify the gapped nodal line as the main source of the giant AHE in $Co_3Sn_2S_2$. Facilitated by far-infrared MOKE spectroscopy, we observe a low-energy magneto-optical resonance. As the zero-energy extrapolation of this interband

transition captures the static Hall conductivity, we confirm that the AHE is dominantly intrinsic. Our *ab initio* calculations are able to reproduce the experimental spectra with remarkable accuracy, allowing a momentum and band decomposition of the optical Hall conductivity. We find that the Weyl points located 60 meV above the Fermi energy only yield singular contributions in small k volumes. By contrast, the nodal line segments approaching or crossing the Fermi energy produce large AHE hot spots after being gapped by SOC. In addition, we verify that the tilt of the nodal line is a crucial factor, producing the strong nodal-line resonance observed here, but can also lead to pairwise cancellation. Remarkably, the linear dichroism is significantly enhanced by the nodal-line resonance, providing a potentially new spectroscopic indicator of topological states. Finally, we note that this magneto-optical analysis is not restricted to Weyl semimetals but applicable for a broad material platform, where large AHE is suspected to originate from topological bands. Since in magnetic materials the electronic topology may couple to the magnetic order, it is also a suitable tool to monitor the effects of, e.g., external fields for manipulating topological properties, which is hardly accessible for other spectroscopy techniques including ARPES.

ACKNOWLEDGMENTS

The authors are grateful to Wei-Kuo Li, Joachim Deisenhofer, Christine Kuntscher, Liviu Chioncel, and Artem Pronin for fruitful discussions. This work was supported by the Hungarian National Research, Development and Innovation Office–NKFIH Grants No. FK 135003 and No. Bolyai 00318/20/11 and by the Ministry of Innovation and Technology and the National Research, Development and Innovation Office within the Quantum Information National Laboratory of Hungary, by the National Science and Technology Council in Taiwan and by the Deutsche Forschungsgemeinschaft (DFG, German Research Foundation) – TRR 360 – 492547816. S.B. is supported by the UNKP-22-5-BME-280 New National Excellence Program of the Ministry for Innovation and Technology from the source of the National Research, Development and Innovation Fund.

[1] N. P. Armitage, E. J. Mele, and A. Vishwanath, Weyl and Dirac semimetals in three-dimensional solids, Rev. Mod. Phys. **90**, 015001 (2018).

[2] A. A. Burkov, M. D. Hook, and L. Balents, Topological nodal semimetals, Phys. Rev. B **84**, 235126 (2011).

[3] B. Bradlyn, J. Cano, Z. Wang, M. G. Vergniory, C. Felser, R. J. Cava, and B. A. Bernevig, Beyond Dirac and Weyl fermions: Unconventional quasiparticles in conventional crystals, Science **353**, aaf5037 (2016).

[4] T. Bzdušek, Q. S. Wu, A. Rüegg, M. Sigrist, and A. A. Soluyanov, Nodal-chain metals, Nature (London) **538**, 75 (2016).

[5] M. A. Wilde, M. Dodenhöft, A. Niedermayr, A. Bauer, M. M. Hirschmann, K. Alpin, A. P. Schnyder, and C. Pfleiderer, Symmetry-enforced topological nodal planes at the Fermi surface of a chiral magnet, Nature (London) **594**, 374 (2021).

[6] T. Liang, Q. Gibson, M. N. Ali, M. Liu, R. J. Cava, and N. P. Ong, Ultrahigh mobility and giant magnetoresistance in the Dirac semimetal Cd_3As_2, Nat. Mater. **14**, 280 (2015).

[7] C. Shekhar, A. K. Nayak, Y. Sun, M. Schmidt, M. Nicklas, I. Leermakers, U. Zeitler, Y. Skourski, J. Wosnitza, Z. Liu, Y. Chen, W. Schnelle, H. Borrmann, Y. Grin, C. Felser, and B. Yan, Extremely large magnetoresistance and ultrahigh mobility in the topological Weyl semimetal candidate NbP, Nat. Phys. **11**, 645 (2015).

[8] J. Xiong, S. K. Kushwaha, T. Liang, J. W. Krizan, M. Hirschberger, W. Wang, R. J. Cava, and N. P. Ong, Evidence for the chiral anomaly in the Dirac semimetal Na_3Bi, Science **350**, 413 (2015).

[9] X. Huang, L. Zhao, Y. Long, P. Wang, D. Chen, Z. Yang, H. Liang, M. Xue, H. Weng, Z. Fang, X. Dai, and G. Chen, Observation of the Chiral-Anomaly-Induced Negative Magnetoresistance in 3D Weyl Semimetal TaAs, Phys. Rev. X **5**, 031023 (2015).

[10] Z. K. Liu, B. Zhou, Y. Zhang, Z. J. Wang, H. M. Weng, D. Prabhakaran, S.-K. Mo, Z. X. Shen, Z. Fang, X. Dai, Z. Hussain, and Y. L. Chen, Discovery of a three-dimensional topological Dirac semimetal, Na_3Bi, Science **343**, 864 (2014).

[11] Z. K. Liu, J. Jiang, B. Zhou, Z. J. Wang, Y. Zhang, H. M. Weng, D. Prabhakaran, S.-K. Mo, H. Peng, P. Dudin, T. Kim, M. Hoesch, Z. Fang, X. Dai, Z. X. Shen, D. L. Feng, Z. Hussain, and Y. L. Chen, A stable three-dimensional topological Dirac semimetal Cd_3As_2, Nat. Mater. **13**, 677 (2014).

[12] S.-Y. Xu, C. Liu, S. K. Kushwaha, R. Sankar, J. W. Krizan, I. Belopolski, M. Neupane, G. Bian, N. Alidoust, T.-R. Chang, H.-T. Jeng, C.-Y. Huang, W.-F. Tsai, H. Lin, P. P. Shibayev, F.-C. Chou, R. J. Cava, and M. Z. Hasan, Observation of Fermi arc surface states in a topological metal, Science **347**, 294 (2015).

[13] I. Belopolski, K. Manna, D. S. Sanchez, G. Chang, B. Ernst, J. Yin, S. S. Zhang, T. Cochran, N. Shumiya, H. Zheng, B. Singh, G. Bian, D. Multer, M. Litskevich, X. Zhou, S. M. Huang, B. Wang, T. R. Chang, S. Y. Xu, A. Bansil *et al.*, Discovery of topological Weyl fermion lines and drumhead surface states in a room temperature magnet, Science **365**, 1278 (2019).

[14] X. Yuan, Z. Yan, C. Song, M. Zhang, Z. Li, C. Zhang, Y. Liu, W. Wang, M. Zhao, Z. Lin, T. Xie, J. Ludwig, Y. Jiang, X. Zhang, C. Shang, Z. Ye, J. Wang, F. Chen, Z. Xia, D. Smirnov *et al.*, Chiral Landau levels in Weyl semimetal NbAs with multiple topological carriers, Nat. Commun. **9**, 1854 (2018).

[15] M. Zhao, Z. Yan, X. Xie, Y. Yang, P. Leng, M. Ozerov, D. Yan, Y. Shi, J. Yang, F. Xiu, and S. Dong, Unconventional Landau level transitions in Weyl semimetal NbP, Phys. Rev. Mater. **6**, 054204 (2022).

[16] G. Chang, B. Singh, S. Y. Xu, G. Bian, S. M. Huang, C. H. Hsu, I. Belopolski, N. Alidoust, D. S. Sanchez, H. Zheng, H. Lu, X. Zhang, Y. Bian, T. R. Chang, H. T. Jeng, A. Bansil, H. Hsu, S. Jia, T. Neupert, H. Lin *et al.*, Magnetic and noncentrosymmetric Weyl fermion semimetals in the RAlGe family of compounds (R = rare earth), Phys. Rev. B **97**, 041104(R) (2018).

[17] J.-X. Yin, S. S. Zhang, H. Li, K. Jiang, G. Chang, B. Zhang, B. Lian, C. Xiang, I. Belopolski, H. Zheng, T. A. Cochran, S.-Y. Xu, G. Bian, K. Liu, T.-R. Chang, H. Lin, Z.-Y. Lu, Z. Wang,

S. Jia, W. Wang *et al.*, Giant and anisotropic many-body spin-orbit tunability in a strongly correlated kagome magnet, Nature (London) **562**, 91 (2018).

[18] Y. Li, Q. Wang, L. DeBeer-Schmitt, Z. Guguchia, R. D. Desautels, J. X. Yin, Q. Du, W. Ren, X. Zhao, Z. Zhang, I. A. Zaliznyak, C. Petrovic, W. Yin, M. Z. Hasan, H. Lei, and J. M. Tranquada, Magnetic-Field Control of Topological Electronic Response Near Room Temperature in Correlated Kagome Magnets, Phys. Rev. Lett. **123**, 196604 (2019).

[19] K. Ueda, J. Fujioka, Y. Takahashi, T. Suzuki, S. Ishiwata, Y. Taguchi, M. Kawasaki, and Y. Tokura, Anomalous domain-wall conductance in pyrochlore-type $Nd_2Ir_2O_7$ on the verge of the metal-insulator transition, Phys. Rev. B **89**, 075127 (2014).

[20] D. Destraz, L. Das, S. S. Tsirkin, Y. Xu, T. Neupert, J. Chang, A. Schilling, A. G. Grushin, J. Kohlbrecher, L. Keller, P. Puphal, E. Pomjakushina, and J. S. White, Magnetism and anomalous transport in the Weyl semimetal PrAlGe: Possible route to axial gauge fields, npj Quantum Mater. **5**, 5 (2020).

[21] A. A. Burkov and L. Balents, Weyl Semimetal in a Topological Insulator Multilayer, Phys. Rev. Lett. **107**, 127205 (2011).

[22] N. Nagaosa, J. Sinova, S. Onoda, A. H. MacDonald, and N. P. Ong, Anomalous Hall effect, Rev. Mod. Phys. **82**, 1539 (2010).

[23] E. Liu, Y. Sun, N. Kumar, L. Muechler, A. Sun, L. Jiao, S.-y. Yang, D. Liu, A. Liang, Q. Xu, J. Kroder, V. Süß, H. Borrmann, C. Shekhar, Z. Wang, C. Xi, W. Wang, W. Schnelle, S. Wirth, Y. Chen *et al.*, Giant anomalous Hall effect in a ferromagnetic kagome-lattice semimetal, Nat. Phys. **14**, 1125 (2018).

[24] C. Fang, H. Weng, X. Dai, and Z. Fang, Topological nodal line semimetals, Chin. Phys. B **25**, 117106 (2016).

[25] S. Y. Yang, H. Yang, E. Derunova, S. S. Parkin, B. Yan, and M. N. Ali, Symmetry demanded topological nodal-line materials, Adv. Phys.: X **3**, 1414631 (2018).

[26] M. Zabel, S. Wandinger, and K.-J. Range, Ternary chalcogenides $M_3M'_2X_2$ with Shandite-type structure, Z. Naturforsch. **34**, 238 (1979).

[27] M. A. Kassem, Y. Tabata, T. Waki, and H. Nakamura, Low-field anomalous magnetic phase in the kagome-lattice Shandite $Co_3Sn_2S_2$, Phys. Rev. B **96**, 014429 (2017).

[28] Z. Guguchia, J. A. Verezhak, D. J. Gawryluk, S. S. Tsirkin, J. X. Yin, I. Belopolski, H. Zhou, G. Simutis, S. S. Zhang, T. A. Cochran, G. Chang, E. Pomjakushina, L. Keller, Z. Skrzeczkowska, Q. Wang, H. C. Lei, R. Khasanov, A. Amato, S. Jia, T. Neupert *et al.*, Tunable anomalous Hall conductivity through volume-wise magnetic competition in a topological kagome magnet, Nat. Commun. **11**, 559 (2020).

[29] C. Lee, P. Vir, K. Manna, C. Shekhar, J. E. Moore, M. A. Kastner, C. Felser, and J. Orenstein, Observation of a phase transition within the domain walls of ferromagnetic $Co_3Sn_2S_2$, Nat. Commun. **13**, 6 (2022).

[30] J. R. Soh, C. J. Yi, I. Zivkovic, N. Qureshi, A. Stunault, B. Ouladdiaf, J. A. Rodríguez-Velamazán, Y. G. Shi, H. M. Rønnow, and A. T. Boothroyd, Magnetic structure of the topological semimetal $Co_3Sn_2S_2$, Phys. Rev. B **105**, 094435 (2022).

[31] J.-x. Yin, S. S. Zhang, G. Chang, Q. Wang, S. S. Tsirkin, Z. Guguchia, B. Lian, H. Zhou, K. Jiang, I. Belopolski, N. Shumiya, D. Multer, M. Litskevich, T. A. Cochran, H. Lin, Z. Wang, T. Neupert, S. Jia, H. Lei, and M. Z. Hasan, Negative flat band magnetism in a spin-orbit-coupled correlated kagome magnet, Nat. Phys. **15**, 443 (2019).

[32] Y. Xu, J. Zhao, C. Yi, Q. Wang, Q. Yin, Y. Wang, X. Hu, L. Wang, E. Liu, G. Xu, L. Lu, A. A. Soluyanov, H. Lei, Y. Shi, J. Luo, and Z.-G. Chen, Electronic correlations and flattened band in magnetic Weyl semimetal candidate $Co_3Sn_2S_2$, Nat. Commun. **11**, 3985 (2020).

[33] Q. Wang, Y. Xu, R. Lou, Z. Liu, M. Li, Y. Huang, D. Shen, H. Weng, S. Wang, and H. Lei, Large intrinsic anomalous Hall effect in half-metallic ferromagnet $Co_3Sn_2S_2$ with magnetic Weyl fermions, Nat. Commun. **9**, 3681 (2018).

[34] S. Minami, F. Ishii, M. Hirayama, T. Nomoto, T. Koretsune, and R. Arita, Enhancement of the transverse thermoelectric conductivity originating from stationary points in nodal lines, Phys. Rev. B **102**, 205128 (2020).

[35] I. Belopolski, T. A. Cochran, X. Liu, Z.-J. Cheng, X. P. Yang, Z. Guguchia, S. S. Tsirkin, J.-X. Yin, P. Vir, G. S. Thakur, S. S. Zhang, J. Zhang, K. Kaznatcheev, G. Cheng, G. Chang, D. Multer, N. Shumiya, M. Litskevich, E. Vescovo, T. K. Kim *et al.*, Signatures of Weyl Fermion Annihilation in a Correlated Kagome Magnet, Phys. Rev. Lett. **127**, 256403 (2021).

[36] D. F. Liu, A. J. Liang, E. K. Liu, Q. N. Xu, Y. W. Li, C. Chen, D. Pei, W. J. Shi, S. K. Mo, P. Dudin, T. Kim, C. Cacho, G. Li, Y. Sun, L. X. Yang, Z. K. Liu, S. S. Parkin, C. Felser, and Y. L. Chen, Magnetic Weyl semimetal phase in a Kagomé crystal, Science **365**, 1282 (2019).

[37] D. F. Liu, E. K. Liu, Q. N. Xu, J. L. Shen, Y. W. Li, D. Pei, A. J. Liang, P. Dudin, T. K. Kim, C. Cacho, Y. F. Xu, Y. Sun, L. X. Yang, Z. K. Liu, C. Felser, S. S. Parkin, and Y. L. Chen, Direct observation of the spin-orbit coupling effect in magnetic Weyl semimetal $Co_3Sn_2S_2$, npj Quantum Mater. **7**, 1 (2022).

[38] S. Howard, L. Jiao, Z. Wang, N. Morali, R. Batabyal, P. Kumar-Nag, N. Avraham, H. Beidenkopf, P. Vir, E. Liu, C. Shekhar, C. Felser, T. Hughes, and V. Madhavan, Evidence for one-dimensional chiral edge states in a magnetic Weyl semimetal $Co_3Sn_2S_2$, Nat. Commun. **12**, 1 (2021).

[39] Q. Wang, S. Sun, X. Zhang, F. Pang, and H. Lei, Anomalous Hall effect in a ferromagnetic Fe_3Sn_2 single crystal with a geometrically frustrated Fe bilayer kagome lattice, Phys. Rev. B **94**, 075135 (2016).

[40] L. Ye, M. Kang, J. Liu, F. von Cube, C. R. Wicker, T. Suzuki, C. Jozwiak, A. Bostwick, E. Rotenberg, D. C. Bell, L. Fu, R. Comin, and J. G. Checkelsky, Massive Dirac fermions in a ferromagnetic kagome metal, Nature (London) **555**, 638 (2018).

[41] F. Schilberth, N. Unglert, L. Prodan, F. Meggle, J. Ebad Allah, C. A. Kuntscher, A. A. Tsirlin, V. Tsurkan, J. Deisenhofer, L. Chioncel, I. Kézsmárki, and S. Bordács, Magneto-optical detection of topological contributions to the anomalous Hall effect in a kagome ferromagnet, Phys. Rev. B **106**, 144404 (2022).

[42] M. Holder, Y. S. Dedkov, A. Kade, H. Rosner, W. Schnelle, A. Leithe-Jasper, R. Weihrich, and S. L. Molodtsov, Photoemission study of electronic structure of the half-metallic ferromagnet $Co_3Sn_2S_2$, Phys. Rev. B **79**, 205116 (2009).

[43] M. A. Kassem, Y. Tabata, T. Waki, and H. Nakamura, Single crystal growth and characterization of kagomé-lattice shandites $Co_3Sn_{2-x}In_xS_2$, J. Cryst. Growth **426**, 208 (2015).

[44] M. A. Kassem, Y. Tabata, T. Waki, and H. Nakamura, Unconventional critical behaviors at the magnetic phase transition of $Co_3Sn_2S_2$ kagomé ferromagnet, J. Phys.: Condens. Matter **33**, 015801 (2020).

[45] K. Sato, Measurement of magneto-optical Kerr effect using piezo-birefringent modulator, Jpn. J. Appl. Phys. **20**, 2403 (1981).

[46] L. Demkó, G. A. H. Schober, V. Kocsis, M. S. Bahramy, H. Murakawa, J. S. Lee, I. Kézsmárki, R. Arita, N. Nagaosa, and Y. Tokura, Enhanced Infrared Magneto-Optical Response of the Nonmagnetic Semiconductor BiTeI Driven by Bulk Rashba Splitting, Phys. Rev. Lett. **109**, 167401 (2012).

[47] S. Bordács, I. Kézsmárki, K. Ohgushi, and Y. Tokura, Experimental band structure of the nearly half-metallic $CuCr_2Se_4$: An optical and magneto-optical study, New J. Phys. **12**, 053039 (2010).

[48] G. Kresse and J. Furthmüller, Efficiency of *ab-initio* total energy calculations for metals and semiconductors using a plane-wave basis set, Comput. Mater. Sci. **6**, 15 (1996).

[49] G. Kresse and J. Furthmüller, Efficient iterative schemes for *ab initio* total-energy calculations using a plane-wave basis set, Phys. Rev. B **54**, 11169 (1996).

[50] G. Kresse and D. Joubert, From ultrasoft pseudopotentials to the projector augmented-wave method, Phys. Rev. B **59**, 1758 (1999).

[51] J. P. Perdew, M. Ernzerhof, and K. Burke, Rationale for mixing exact exchange with density functional approximations, J. Chem. Phys. **105**, 9982 (1996).

[52] P. Vaqueiro and G. G. Sobany, ChemInform abstract: A powder neutron diffraction study of the metallic ferromagnet $Co_3Sn_2S_2$, Chem. Inf. **40** (2009).

[53] G. Pizzi, V. Vitale, R. Arita, S. Blügel, F. Freimuth, G. Géranton, M. Gibertini, D. Gresch, C. Johnson, T. Koretsune, J. Ibañez-Azpiroz, H. Lee, J.-M. Lihm, D. Marchand, A. Marrazzo, Y. Mokrousov, J. I. Mustafa, Y. Nohara, Y. Nomura, L. Paulatto *et al.*, Wannier90 as a community code: new features and applications, J. Phys.: Condens. Matter **32**, 165902 (2020).

[54] R. Yang, T. Zhang, L. Zhou, Y. Dai, Z. Liao, H. Weng, and X. Qiu, Magnetization-Induced Band Shift in Ferromagnetic Weyl Semimetal $Co_3Sn_2S_2$, Phys. Rev. Lett. **124**, 077403 (2020).

[55] Y. Okamura, S. Minami, Y. Kato, Y. Fujishiro, Y. Kaneko, J. Ikeda, J. Muramoto, R. Kaneko, K. Ueda, V. Kocsis, N. Kanazawa, Y. Taguchi, T. Koretsune, K. Fujiwara, A. Tsukazaki, R. Arita, Y. Tokura, and Y. Takahashi, Giant magneto-optical responses in magnetic Weyl semimetal $Co_3Sn_2S_2$, Nat. Commun. **11**, 4619 (2020).

[56] I. Kézsmárki, G. Mihály, R. Gaál, N. Barisić, A. Akrap, H. Berger, L. Forró, C. C. Homes, and L. Mihály, Separation of Orbital Contributions to the Optical Conductivity of $BaVS_3$, Phys. Rev. Lett. **96**, 186402 (2006).

[57] The obtained band structure along general high-symmetry points is shown in Fig. S2(a).

[58] M.-C. Jiang and G.-Y. Guo, Large magneto-optical effect and magnetic anisotropy energy in two-dimensional metallic ferromagnet Fe_3GeTe_2, Phys. Rev. B **105**, 014437 (2022).

[59] See Supplemental Material at http://link.aps.org/supplemental/10.1103/PhysRevB.107.214441 for the experimental and theoretical details.

[60] M. Kanagaraj, J. Ning, and L. He, Topological $Co_3Sn_2S_2$ magnetic Weyl semimetal: From fundamental understanding to diverse fields of study, Rev. Phys. **8**, 100072 (2022).

[61] J. F. Steiner, A. V. Andreev, and D. A. Pesin, Anomalous Hall Effect in Type-I Weyl Metals, Phys. Rev. Lett. **119**, 036601 (2017).

[62] K. Sonowal, A. Singh, and A. Agarwal, Giant optical activity and Kerr effect in type-I and type-II Weyl semimetals, Phys. Rev. B **100**, 085436 (2019).

[63] V. Antonov, B. Harmon, and A. Yaresko, *Electronic Structure and Magneto-Optical Properties of Solids* (Kluwer Academic, Dordrecht, 2004).